polysaccharides

MDPI

Article

Hemostatic Dressings Made of Oxidized Bacterial Nanocellulose Membranes

E. C. Queirós [1,2], S. P. Pinheiro [1], J. E. Pereira [3], J. Prada [3], I. Pires [3], F. Dourado [1], P. Parpot [1,2] and M. Gama [1,*]

[1] CEB—Centre of Biological Engineering, University of Minho, 4710-057 Braga, Portugal; eugeniaqueiros@ceb.uminho.pt (E.C.Q.); sarapspinheiro@gmail.com (S.P.P.); fdourado@deb.uminho.pt (F.D.); parpot@quimica.uminho.pt (P.P.)
[2] CQUM—Centre of Chemistry, University of Minho, 4710-057 Braga, Portugal
[3] CECAV—Veterinary and Animal Research Centre, University of Trás-os-Montes and Alto Douro, Quinta de Prados, 5000-801 Vila Real, Portugal; jeduardo@utad.pt (J.E.P.); jprada@utad.pt (J.P.); ipiress@utad.pt (I.P.)
* Correspondence: fmgama@deb.uminho.pt

Abstract: Surgicel® (regenerated oxidized cellulose) is a bio-absorbable hemostatic material widely applied to prevent surgery-derived adhesions. Some critical issues have been reported associated with this biomaterial, which we aimed to overcome by producing bacterial nanocellulose (BNC) membranes with hemostatic activity, through electrochemical oxidation using the tetramethylpiperidine-1-oxyl (TEMPO) radical. Samples were characterized by FTIR, NMR, SEM, XRD and their degree of polymerization. The oxidation degree was evaluated by titration of the carboxyl groups and the hemostatic behavior by whole-blood-clotting assays. In vitro and in vivo biodegradability of oxidized BNC membranes were evaluated and compared with that of Surgicel®. The oxidation degree increased from 4% to 7% and up to 15%, corresponding to an applied charge of 400, 700 and 1200 Coulombs, respectively. The oxidized BNC preserved the crystallinity and the 3D nano-fibrillar network, and demonstrated hemostatic activity, although not as effective as that of Surgicel®. In vivo assays demonstrated that the oxidized membranes did not induce an inflammatory response, revealing a good biocompatibility. However, non-degraded oxidized BNC was still detected at the implantation site after 56 days.

Keywords: bacterial nanocellulose; hemostatic dressings; cellulose biodegradability

Citation: Queirós, E.C.; Pinheiro, S.P.; Pereira, J.E.; Prada, J.; Pires, I.; Dourado, F.; Parpot, P.; Gama, M. Hemostatic Dressings Made of Oxidized Bacterial Nanocellulose Membranes. *Polysaccharides* **2021**, *2*, 80–99. https://doi.org/polysaccharides2010006

Received: 8 December 2020
Accepted: 2 February 2021
Published: 19 February 2021

1. Introduction

Hemostasis involves a complex interaction between four key elements: the vascular endothelium, platelets, the coagulation pathway and fibrinolysis. When the natural physiologic hemostasis is not enough to control a hemorrhagic episode, it is essential to use hemostatic materials. Different hemostatic approaches may be applied according to the type of injury, and they can be constituted of materials based on polyethylene glycol [1,2], regenerated oxidized cellulose (Surgicel®) [3] or proteins like thrombin, collagen (Colgel®) and fibrin (TachoSil®) [4,5]. Surgicel®, made by Ethicon Inc. of Johnson & Johnson, is a bio-absorbable material widely applied for intraoperative hemostasis and adhesion prevention in surgery. Surgicel®seems to act as a mesh for platelet adhesion and aggregation, helping the formation of an artificial clot, while its negative charge is likely to activate the secondary hemostasis as well. It is advisable to remove Surgicel® when the hemostasis is controlled. However, the most common procedure is to leave the hemostatic in situ to reabsorb spontaneously, usually without any secondary effects. If left in situ, the complete degradation should occur between four and eight weeks [6,7]. Nevertheless, some issues were reported associated with the use of Surgicel®. The presence of a recurrent gastrointestinal stromal tumor four months after surgical resection was ascribed to the intra-abdominal foreign-body granuloma caused by the presence of Surgicel® residues in an 83-year-old male patient [7]. Another case reported the formation of a foreign-body

reaction, contributing to the development of an intracranial giant-cell granuloma. In this case, the patient was diagnosed with intracranial hemorrhage that was ascribed to the use of Surgicel® [8,9]. It is thus essential to develop new hemostatic dressings able to overcome these drawbacks.

Bacterial nanocellulose (BNC) represents an alternative source of cellulose with great potential for some specific applications, given its very special technical properties [10,11]. BNC has good mechanical properties (Young's modulus around 15–35 GPa and tensile strength of 200–300 MPa), a high crystallinity, a high degree of polymerization and a high water content—up to 200 times its dry weight [10,12,13]. In addition, BNC is a biocompatible material that exhibits high purity since it does not have hemicellulose, pectin and lignin, as its vegetable counterpart. *Komagataeibacter xylinus* [14] is the most efficient producer, and depending on the cultivation method and the bioreactor used, BNC may be produced in different shapes such as membranes, hollow tubes, pellets or thin fibrous materials. When cultivated in static culture, a nanofibrillar pellicle is obtained, where one side displays a denser surface, while the other one exhibits a gelatinous layer [15,16]. Some BNC-based materials are commercially available for biomedical applications, e.g., as wound dressings, such as CelMat®, EpiProtect® and Nanoskin®. The excellent biocompatibility of BNC has been demonstrated in several works. For instance, Helenius et al. assessed the in vivo biocompatibility through subcutaneous implantation in rats for one, four and 12 weeks. The chronic inflammation, foreign body responses, cell ingrowth and angiogenesis were evaluated through histology, immunohistochemistry and electron microscopy. The obtained results showed that there was no macroscopic or microscopic evidence of inflammation around the implants. There also were no signs of fibrotic capsule or giant cells, and the BNC was well integrated into the host tissue and did not induce any chronic inflammatory reactions [17]. Pértile et al. also showed the good biocompatibility of BNC in a long-term biocompatibility study. The BNC samples were implanted in mice, and it was shown that a mild and benign inflammatory reaction occurred that decreased over time and did not induce a foreign-body reaction. Furthermore, there were no signs of chronic inflammatory reaction or encapsulation, while the formation of new blood vessels around and inside the implants was observed [18]. More recently, Zhang et al. evaluated the in vitro biocompatibility of a BNC scaffold for corneal stroma replacement, through the culture of rabbit corneal epithelial and stromal cells on the BNC scaffold, during a three-month follow-up. The obtained results showed that BNC supported cell adhesion, proliferation and differentiation. On the other hand, in vivo tests further confirmed the good biocompatibility and stability of BNC in rabbit cornea, making BNC an attractive option for tissue engineering of corneal stroma [19]. Beyond biocompatibility, in the biomedical field, another desirable requirement for many applications is biodegradability. The modification of BNC in order to increase and improve its biodegradability has been attempted. Thus, an improvement in biodegradation may be achieved through oxidation, making BNC resorbable by the organism [20,21].

The chemical modification of BNC can be achieved through the carboxylic functionalization on C2, C3 and C6 of the glucose residue. In this process, the hydroxyl group at C2, C3 and C6 is first oxidized into an aldehyde, which in turn is further oxidized into a carboxylic group [22]. Oxidation is commonly accompanied by degradation and a concomitant decrease in the degree of polymerization, which can be a consequence of the oxidation reaction per se, or can be triggered by subsequent pH changes. The 2,2,6,6-Tetramethylpiperidine-1-oxyl (TEMPO) has been widely applied to oxidized cellulose. In the last few years, TEMPO has been chosen as the primary method to convert polysaccharides into the corresponding polyuronic acids through the selective oxidation of the primary hydroxyl groups at C6 to carboxyl groups [23,24]. During the process, TEMPO is oxidized through a one-electron transfer reaction to the corresponding oxoammonium (active oxidant in the primary alcohol oxidation). Furthermore, the electrooxidation of the hydroxylamine regenerating the $TEMPO^{+}$ occurs at the anode in situ. This approach is cleaner than the alternative chemical method, which use co-oxidants like NaClO-NaBr

or water-acetonitrile-NaClO-$NaClO_2$ [25]. Moreover, contrarily to the enzymatic or metal catalyzed oxidation, the TEMPO-oxidation method is very efficient in the conversion of high-molecular-weight polysaccharides [26]. Furthermore, TEMPO is also characterized by its stability, non-toxicity and non-mutagenic features [27], as well as its high reaction rate and yield, allowing a controlled modification of the polysaccharides [26]. Thus, the oxidation of cellulose by the TEMPO radical may be used to facilitate the mechanical disintegration of cellulose fibers into nano fibrils, reducing energy and mechanical action. Unreacted TEMPO may be recovered from the reaction medium after the removal of $NaHCO_3$ and Na_2CO_3 (carbonate buffer) through neutralization using a cation exchange resin. When an electrochemical oxidation carbonate buffer is used as the electrolyte, the increase of ionic strength provides a decrease in the internal resistance of the electrochemical cell [28].

We aimed at oxidizing BNC through electrochemical methods in order to increase its biodegradability, while conferring hemostatic properties. Since BNC fibers are ultrathin, we hypothesize that surface oxidation may lead to a substantial improvement of the biodegradability of the BNC fibers. While the hemostatic behavior was achieved after oxidation, the in vivo degradability was not satisfactory, despite the good biocompatibility of the oxidized BNC membranes.

2. Materials and Methods

2.1. BNC Membranes Purification

Commercial BNC membranes (purchased from HTK CO., LTD, Ho Chi Minh City, Vietnam) with an initial thickness of 12–15 mm were washed once with distilled water and then with 5% (*w*/*v*) of sodium dodecyl sulphate (SDS; Sigma-Aldrich, St. Louis, MO, USA), to remove endotoxins for five days (solution renewed every day), followed by extensive washing with distilled water. All washings were done at room temperature. Afterward, the membranes were sliced to a final thickness of 3.3 mm and then sterilized by autoclaving at 121 °C for 20 min, prior to storage in distilled water at 4 °C. For all the characterization tests, BNC membranes were then frozen at −80°C and freeze-dried at −100 °C (Scanvac Coolsafe) for five days.

2.2. Electrochemical Setup

Cyclic voltammetry (CV) and constant-potential electrolysis were the applied electrochemical techniques. The electrolysis was carried out in aqueous solution using the TEMPO radical (Sigma-Aldrich) and 0.2 M of carbonate buffer ($NaHCO_3$ and Na_2CO_3) (pH = 10). CV was performed at a constant scanning speed of 50 mV s^{-1} to assess the oxidation-reduction process.

The voltammetric study was performed in a thermostated three-electrode and two-compartment glass cell separated by an ion-exchange membrane (Nafion 417). Toray carbon paper was used as working electrode. A tap was introduced into the Luggin bridge in order to establish the contact between the reference and the electrolyte solutions without any contamination of the latter by the ions of the reference-electrode solution. A saturated calomel electrode (SCE) and a platinum foil (99.95%) were used as the reference and counter electrodes, respectively. Before each experiment, the solutions were deaerated with ultrapure nitrogen (U Quality from Air Liquide), and the nitrogen stream was maintained over the solution during the measurements. The electrochemical instrumentation consisted of a potentiostat/galvanostat from Amel Instruments coupled to a microcomputer through an AD/DA converter. The Labview software (National Instruments) and a PCI-MIO-16E-4 I/O module were used for generating and applying the potential program, as well as for acquiring data, such as current intensities [28].

2.3. Oxidation Degree

The oxidation degree of BNC was evaluated by titration with sodium hydroxide (NaOH). A potassium hydrogen phthalate ($C_8H_5KO_4$) solution was used to determine

the concentration of NaOH (0.012 M) by titration, using phenolphthalein as an indicator. Freeze-dried oxidized BNC membranes (~100 mg, the exact mass was recorded) were cut into small pieces and dispersed in 30 mL of distilled water, and the pH was adjusted to 2.40 with HCl (1 M). The samples were placed at 4 °C for five days under agitation, and the pH was adjusted again before starting the titration.

The oxidation degree was calculated by the following equation:

$$Oxidation\ degree\ (OD)(\%) = \frac{C \times V \times M}{m} \times 100 \quad (1)$$

where C is the concentration of NaOH (mol/L), V is the volume of NaOH (L) used in the titration (rectified considering the value used in a blank titration (without BCN)), M the molecular weight of the BNC monomer (162 g/mol) and m the dry mass of BNC (g) [29]. The titration was terminated only when protonation equilibrium was achieved and no changes in pH were observed.

2.4. Degree of Polymerization

Both oxidized and non-oxidized freeze-dried BNC membranes (50 mg) were cut into small pieces and mixed with 5 mL of distilled water under agitation for 30 min. Then, 5 mL of cupri-ethylenediamine (CED, Sigma-Aldrich) saturated with copper (II) hydroxide was added, and the mixture was agitated for 60 min and then centrifuged for 5 min at 7000 rcf. Finally, the intrinsic viscosities of the BNC samples were obtained using an Ubbelohde capillary-tube viscometer from Rheotek placed in a water bath at 25 °C. The viscosity values were obtained according to the standard ES ISO 5351:2012 Pulps—Determination of limiting viscosity number in cupri-ethylenediamine (CED) solution. Thus, the viscosity ratio η_{ratio} was calculated using the following equation:

$$\eta_{ratio} = \frac{\eta}{\eta_0} = h \times t \quad (2)$$

where h is the viscometer constant that was determined to be 0.132 s^{-1}, and t is the efflux time (in seconds) of the test solution. The viscosity-averaged degree of polymerization (DP_v) was calculated using the Marl–Houwink–Sakurada equation [30]:

$$[\eta] = K \times DPv^{\alpha} \quad (3)$$

where, for BNC samples, K = 0.0002 and α = 1.9705 [31].

Finally, the molecular mass of BNC was calculated from the relationship:

$$DP_v = \frac{M}{162} \quad (4)$$

where M is the molecular mass of the BNC and 162 (g/mol) equals the molecular mass of an anhydroglucose unit [32]. All the samples were analyzed in triplicate.

2.5. Nuclear Magnetic Resonance Spectroscopy (NMR)

The BNC membranes were analyzed by NMR using a Bruker Avance III 400 wide-bore spectrometer (400 MHz, 1H Larmor frequency). A 4 mm double-resonance MAS probe was employed at 100.6 MHz (13C) Larmor frequency. Oxidized and non-oxidized BNC samples were spun in ZrO_2 rotors using a spinning rate of 12 kHz. ^{13}C-CP/MAS NMR spectra were recorded using a ramp step (varying from 100% to 50% in amplitude using 100 points), with a recycle delay of 5 s, a contact time of 2.0 ms and a 1H 90° excitation pulse of 3.10 µs. All chemical shifts are quoted in parts per million from tetramethylsilane (TMS).

2.6. Attenuated Total Reflectance-Fourier-Transform Infrared Spectroscopy (ATR-FTIR) Analysis

Freeze-dried oxidized and non-oxidized BNC membranes were analyzed using an ALPHA II- Bruker spectrometer (Ettlingen, Germany) with a diamond-composite attenuated

total reflectance (ATR) cell. Data were collected using OPUS software, which is integrated in the FTIR equipment. The measurements were recorded with a wavenumber range from 4000 to 400 cm^{-1}, with a resolution of 4 cm^{-1} and 64 scans per sample. The ATR clamp and platform were cleaned with a cotton swab dampened with isopropyl alcohol and then allowed to dry between the analysis of each coupon. All assays were done in duplicate for each sample.

2.7. Scanning Electron Microscopy (SEM)

Freeze-dried oxidized and non-oxidized BNC membranes morphology was assessed by SEM (FEI Quanta 650 FEG; acceleration voltage from 3–10 kV). Both oxidized and non-oxidized BNC membranes were added to aluminum pin stubs with electrically conductive carbon adhesive tape (PELCO Tabs™), with the excess removed using compressed air. Samples were coated with 2.5 nm of Au for improved conductivity. The analysis was conducted at (3–10 kV) with intensity point. For the quantitative analysis of the length of the fibers, at the least five different fibers were selected using the software ImageJ.

2.8. X-ray Diffraction (XRD)

The crystalline structure was assessed using a PANalytical X'Pert Pro MPD diffractometer equipped with X'Celerator detector and secondary monochromator. Freeze-dried oxidized and non-oxidized BNC membranes were analyzed at room temperature using a CuKα radiation and Bragg-Bentano geometry, 0.017°/step and 100 s/step.

The crystallinity index (*CrI*) Equation (5) was calculated using Segal, Creely, Martin & Conrad (1959) [33] equation, i.e., it was calculated as a function of the maximum intensity of the diffraction peak from the crystalline region (I_{200}), at an angle of 2θ ~ 22.5°, and the minimum intensity from the amorphous region (I_{am}), at an angle of 2θ ~ 18°.

$$CrI\ (\%)\ =\ \frac{(I_{200} - I_{am})}{I_{200}} \tag{5}$$

The apparent crystallite size (CS) in the crystallographic planes (1–10), (110) and (200) were calculated assuming that the crystals exhibited uniform size and shape and using Scherrer's equation:

$$CS\ =\ \frac{K\lambda}{FWHM\cos\theta} \tag{6}$$

where K is a dimensionless factor dependent upon the method used to calculate the amplitude (K = 0.9), λ is the wavelength of the incident X-ray (λ = 0.15 nm), *FWHM* is the width of the diffraction peak at half-maximal height (in radians) and θ is the angle of the diffraction peak of the crystalline phase (Bragg's angle). The diffractograms were analyzed by Rietveld refinement with Powder Cell software.

2.9. In Vitro Degradation of Oxidized BNC Membranes

The degradation of oxidized and non-oxidized BNC membranes was tested in vitro using ultra-pure water at 37 °C. The freeze-dried BNC membranes were cut into pieces weighing between 8 and 12 milligrams (the exact mass was recorded). Then, they were immersed in 2 mL of ultra-pure water in centrifuge tubes. After incubation for 3, 7, 14 and 63 days, the samples were taken out, dried in a woven at 50 °C overnight and weighed. The original mass of each sample was designated as m_i, while the mass after degradation was designated as m_f. Thus, the mass-loss rate was calculated using the following equation [29]:

$$Mass\ loss\ =\ \frac{m_i - m_f}{m_i} \times 100 \tag{7}$$

2.10. Biological Assays and Hemostatic Behavior of BNC Membranes

2.10.1. Preparation of Blood Samples

Whole blood was collected from healthy bovine animals from Izicar–Fábrica do Produtos Porcinos, Lda (Vila Nova de Famalicão, Portugal) using citrated (3.2%) 3 mL vacuum blood-collection tubes (Vacuette, Portugal) and transported on ice.

2.10.2. Whole-Blood-Clotting Times

Three mL of whole blood was placed in each well of a 24-well plate. Then, 300 µL of 0.1 M $CaCl_2$ (Riedel-de Haën) was added to induce clotting, and the mixture was incubated for 0, 5, 10, 15 and 25 min at room temperature, with (i) oxidized BNC membranes; (ii) non-oxidized BNC membranes; (iii) Surgicel® (reference material); (iv) glass microspheres (Ø0.40–0.60 mm, Startorius) (positive control) and (v) bare polystyrene (empty well, negative control). A volume of 100 µL of activated whole blood was collected for each time point, and 2.5 mL of distilled water was added to each well, followed by incubation for 5 min to lyse the red blood cells, which were not trapped in the thrombus, and release hemoglobin. Afterward, the concentration of the released hemoglobin was measured by transferring 200 µL of the supernatant to a 96-well plate and analyzed in a spectrophotometer at λ = 540 nm. In this method, a faster clot formation leads to a faster reduction of the detected absorbance value. All the samples were analyzed in triplicate [34].

2.11. In Vivo Biocompatibility Tests of BNC Membranes

All the procedures were carried out in strict accordance with the recommendations for care and use of laboratory animals of the EU directive (2010/63/EU) and national (Decreto-Lei 113/2013) legislation for animal experimentation and welfare. The experimental procedures were carried out with the approval of the Portuguese competent authority, Direção Geral de Alimentação e Veterinária (DGAV, Lisboa, Portugal), under animal ethic approval number 0421/000/000/2017.

Eighteen Wistar female rats (Charles River Laboratories, Les Oncins, France) weighing approximately 250 g were used in this study. All animals were kept in ventilated humidity- and temperature-controlled rooms with a 12/12-h light/dark cycle. The animals were housed in cages (three animals/cage) with corn kernels, and received food pellets and water ad libitum. All animals were implanted subcutaneously with three untreated BNC disks that were 13 mm in diameter on the left side, and three oxidized BNC disks that were 13 mm in diameter in the right side, on the animal's back. Animals were randomly assigned and blindly divided into three groups. The first group (n = 6) had their implants removed after three days, the second group (n = 6) had their implants removed after 14 days, and the third group (n = 6) had their implants removed after 56 days.

2.11.1. Surgical Procedures

Rats were anaesthetized with ketamine (80 mg/kg) and dexmedetomidine (0.2 mg/kg) by intraperitoneal injection, and then prepared for surgery as follows: the back of the animal, from the neck through the tail, was shaved, antisepticized with chlorhexidine and dried. Bodies were covered with sterile sheets except for the incision line. Three skin incisions (length, 2–3 cm) were made on the midline of the back of the animal. On each side, three subcutaneous pockets (approximately 30 mm) were carefully created using mosquito forceps. The implants were introduced into the pockets without fixation, located 20 mm from the line of incision without touching one another. The soft tissues and the skin were reapproximated with monofilament absorbable synthetic sutures (glyconate USP 5/0). The implant site location was performed by placing a subcutaneous stitch with a non-absorbable suture. An ophthalmologic gel was applied to prevent drying of the eyes. Additionally, buprenorphine (0.05 mg/kg) was administered at the end of the surgical procedure immediately before the wound closure was completed. Postoperative pain control was also carried out with buprenorphine (0.05 mg/kg subcutaneous, twice daily) for two days.

The animals were sacrificed under general anesthesia with a lethal dose of pentobarbital (80 mg/kg), delivered by intracardiac injection. Implants were then carefully removed in conjunction with all surrounding tissues and fixed with 4% neutral buffered formalin. After that, both the oxidized and non-oxidized BNC membranes were fixed in 10% neutral buffered formalin, dehydrated and embedded in paraffin. Cross sections (5 µm) were cut and stained with hematoxylin and eosin (H&E) for cellular infiltration and inflammatory response [35], as described below.

2.11.2. Histological Evaluations

The implants and the surrounding tissue were collected at 3, 14 and 56 days post implantation. Samples were fixed in 10% formalin, paraffin embedded, cut to 5 µm and stained with H&E for histological evaluation. For each sample, the biological response parameters were evaluated at the implant–tissue interface with three high-power fields (×400) by two pathologists, and recorded in an appropriate formulary. All the biological response parameters were evaluated according to the ISO standard 10993-6 (annex E), which included the extent of fibrosis/fibrous capsule (layer in micrometers) and inflammation; degeneration, as determined by changes in tissue morphology; the number and distribution from the material–tissue interface of the inflammatory cell types, namely polymorphonuclear neutrophilic leucocytes (PMN), lymphocytes, plasma cells, macrophages and multinucleated cells; the presence, extent and type of necrosis; and other tissue alterations such as vascularization and fatty infiltration. Based on the scoring system for the parameters, a total value was obtained for each animal in each group [35]. The collected data were submitted to statistical analyses. The data were analyzed with one-way analysis of variance (ANOVA) followed by the Tukey multiple comparisons test, which was used to evaluate the statistical differences between the groups using GraphPad Prism 5.0 software. Differences were considered statistically significant at $p < 0.05$.

3. Results and Discussion

BNC with three different oxidation degrees i.e., 4%, 7% and 15%, corresponding to the generation of 400, 700 and 1200 Coulombs (samples BNC 400C, BNC 700C and BNC 1200C, respectively), were obtained and analyzed by FTIR, SEM and XRD, and for in vitro degradation. However, the more oxidized membranes were very fragile, making their handling quite difficult after preparation. Hence, the BNC 1200C samples were excluded from measurements of the degree of polymerization, NMR analysis and hemostatic assays. Finally, in order to reduce the number of animals, the in vivo biocompatibility tests were performed using only the BNC 700C membranes.

3.1. Cyclic Voltammetry (CV)

Before each electrolysis, a CV study of the BNC oxidation using TEMPO mediator and carbonate buffer electrolyte was performed. Taking into account the preliminary voltammetric study that was carried out, the applied potential values were set between 0.7 and 0.8 V vs. SCE. Electrolysis was carried out three times on the Toray carbon electrode in the presence of BNC and TEMPO. The voltammetric study also was performed with TEMPO, in the absence of the BNC membrane, as well as at the beginning and end of the BNC electrolysis (Figure 1). In addition, CV was also used to evaluate the electroreactivity of TEMPO and its chemical stability.

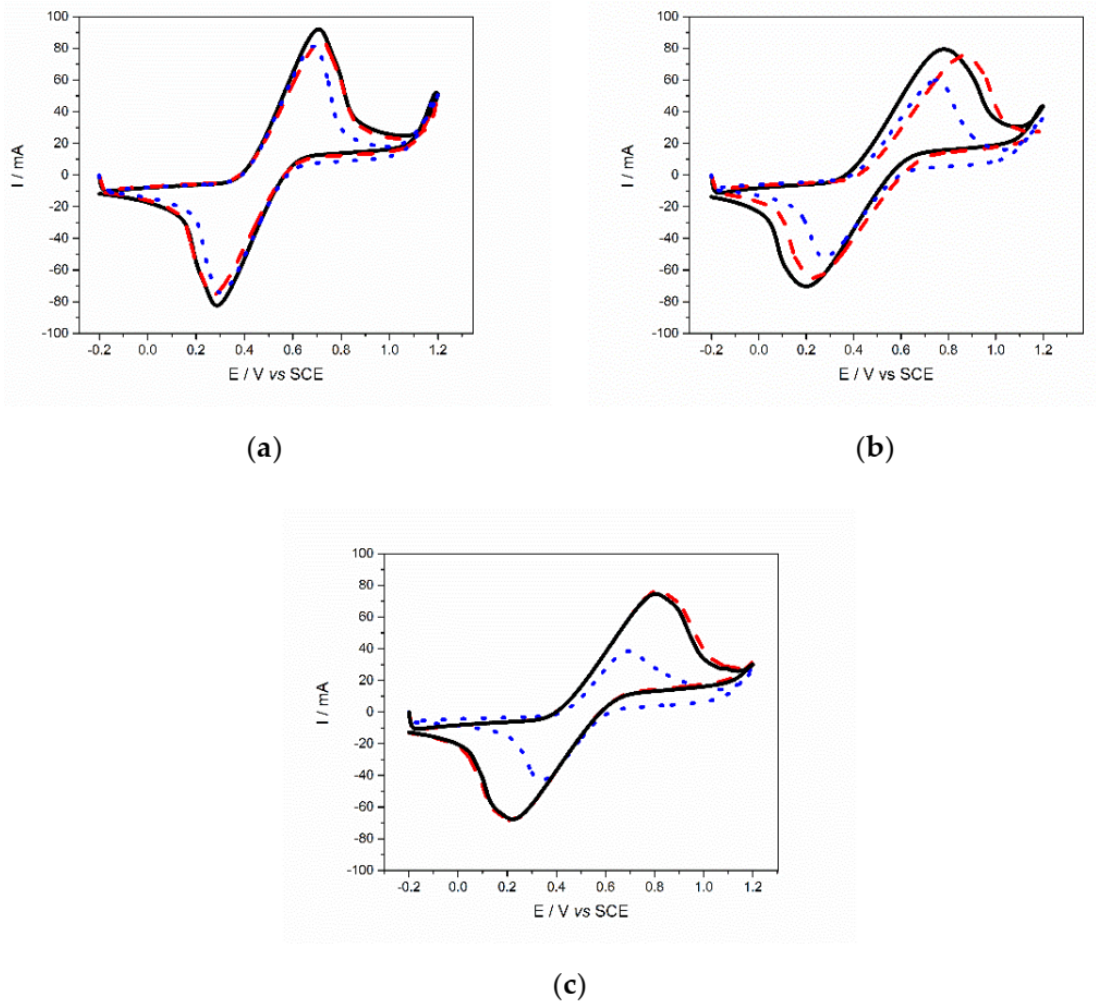

Figure 1. Cyclic voltammograms of the Toray carbon electrode in presence of TEMPO (black line) and of TEMPO with BNC membrane at the beginning (red line) and at the end of the electrolysis (blue line). The voltammograms corresponding to (**a**) BNC 400C, (**b**) BNC 700C and (**c**) BNC 1200C membranes were acquired at room temperature and at a scan rate of 50 mV s^{-1}.

The successively obtained voltammograms remained unchanged, showing the stability of the electrocatalytic materials. Furthermore, they were similar to those obtained by other authors [36–38], and all of them exhibited a characteristic profile and good reversibility, featuring the anodic peak ascribed to the reversible oxidation of TEMPO corresponding to the active oxidant, the ion oxoammonium ($TEMPO^+$), which was reduced into its hydroxylamine form during the cathodic sweep [28]. The current intensities remained almost unchanged after the introduction of the BNC, accompanied by a slight shift in the oxidation potential toward more anodic values. On the other hand, at the end of electrolysis, a decrease in the current intensity was observed in the anodic peak, revealing the oxidation of the BNC membranes. This decrease in the current's intensity also was directly related to an increase in the oxidation degree of the BNC membranes.

3.2. Oxidation Degree

The oxidation degree of the BNC membranes was determined by titration. The values obtained using Equation (1) are shown in Table 1.

Table 1. Oxidation degree (in %) corresponding to different applied charges and the duration of the electrolysis.

Sample	% Oxidation Degree	Duration of Electrolysis (h)
BNC 400C	3.68 ± 1.03	2.39 ± 0.52
BNC 700C	6.45 ± 1.13	6.07 ± 1.25
BNC 1200C	14.92 ± 0.31	14.5 ± 4.94

The results showed that the duration of the electrolysis was proportional to the applied charged, and that roughly, the oxidation degree increased directly with the applied charge (R^2 = 0.98), with the values increasing from 4 to 15% of oxidation depending on the conditions used. These relatively small oxidation degrees were expected, since the reaction occurred only at the surface of the fibers, and the mediator was not able to penetrate the crystalline domains of the cellulose. Moreover, the obtained values were similar to those obtained by Sezer et al. [39], who found that for 6 h of reaction, the oxidation degree was around 7, and for 12 h was approximately 9.

3.3. Degree of Polymerization

The obtained results show that the degree of polymerization decreased with an increase in the oxidation degree, as follows: 1959 ± 63 for non-oxidized BNC, > 1841 ± 36 for BNC 400C and > 1401 ± 65 for BNC 700C. These results are in accordance with other works [31,40–43]. Considering that the inner part of the crystallites is not expected to undergo depolymerization, this must occur to significant extent at the surface level as to lead to the observed average reduction in DP, which justifies the increasing fragility of the membranes as the oxidation increases.

3.4. NMR

NMR was used to confirm the specific oxidation of C6 of the BNC membranes. The obtained spectra are presented in Figure 2.

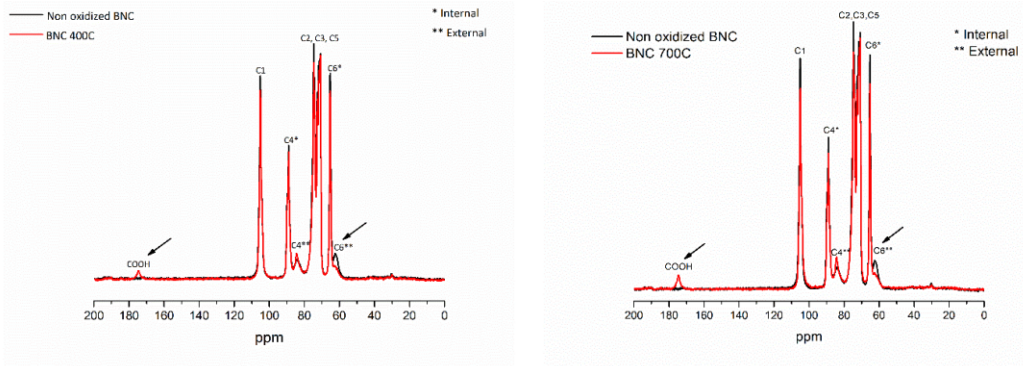

Figure 2. NMR spectra of (**a**) 400C and (**b**) 700C membranes compared with non-oxidized BNC membranes.

The signal at 104.5, 84.5 and 61.7 ppm were assigned to C1, C4 and C6, respectively. However, the peaks between 75.3–70 ppm, corresponding to C2, C3 and C5, were not easily assessed, since the resolution was not good enough [29,44,45]. The peak at 61.7 ppm, related to the C6 primary hydroxyl groups, presented a lower intensity in the oxidized membranes. On the other hand, the peak at 64.9 ppm, corresponding to the C6 primary hydroxyl groups inside the crystalline fibrils and the C2/C3 peaks, remained unchanged as expected, since the hydroxyl groups located in the inner structure of the crystallites hardly suffered oxidation [46]. Finally, the peak around 174.6 ppm, which corresponds to the carboxylate groups produced during the electrolysis, further confirmed the oxidation

of hydroxyl groups [21]. As expected, the intensity of this peak was found to be directly related to the oxidation degree.

3.5. ATR-FTIR

ATR-FTIR spectra of the non-oxidized BNC and different degrees of oxidized BNC are shown in Figure 3. The usual bands ascribed to the chemical structure of BNC were observed: O–H symmetrical stretching around 3350 cm^{-1}; C–H stretching around 2900 cm^{-1}; C–O–C stretching around 1162 cm^{-1}; C–O stretching at 1030 cm^{-1}; and vibration of amorphous cellulose (stretching of the glucose ring) around 899 cm^{-1}. Regarding the oxidized BNC, the most relevant modifications were the appearance of a C=O stretching band at around 1628 cm^{-1} that confirmed the formation of carboxylate groups (–COOH) [23,47]. This peak also confirmed that the hydroxyl groups at the C6 position in the BNC had been successfully converted into carboxyl groups.

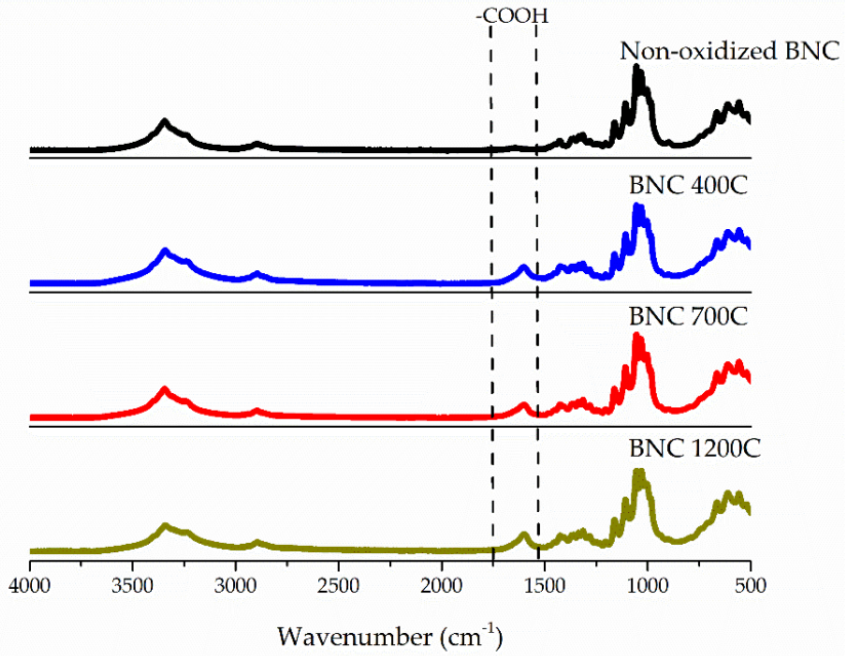

Figure 3. FTIR spectra of oxidized and non-oxidized BNC membranes.

There were no other relevant differences between the spectra of the BNC and oxidized BNC membranes; thus, as it was observed from the NMR analysis, it may be concluded that highly selective oxidation was achieved.

3.6. SEM

The influence of oxidation on BNC membranes morphology was assessed by SEM. The obtained images are presented in Figure 4. The width of the fibers was also measured, and the values are presented in Table 2.

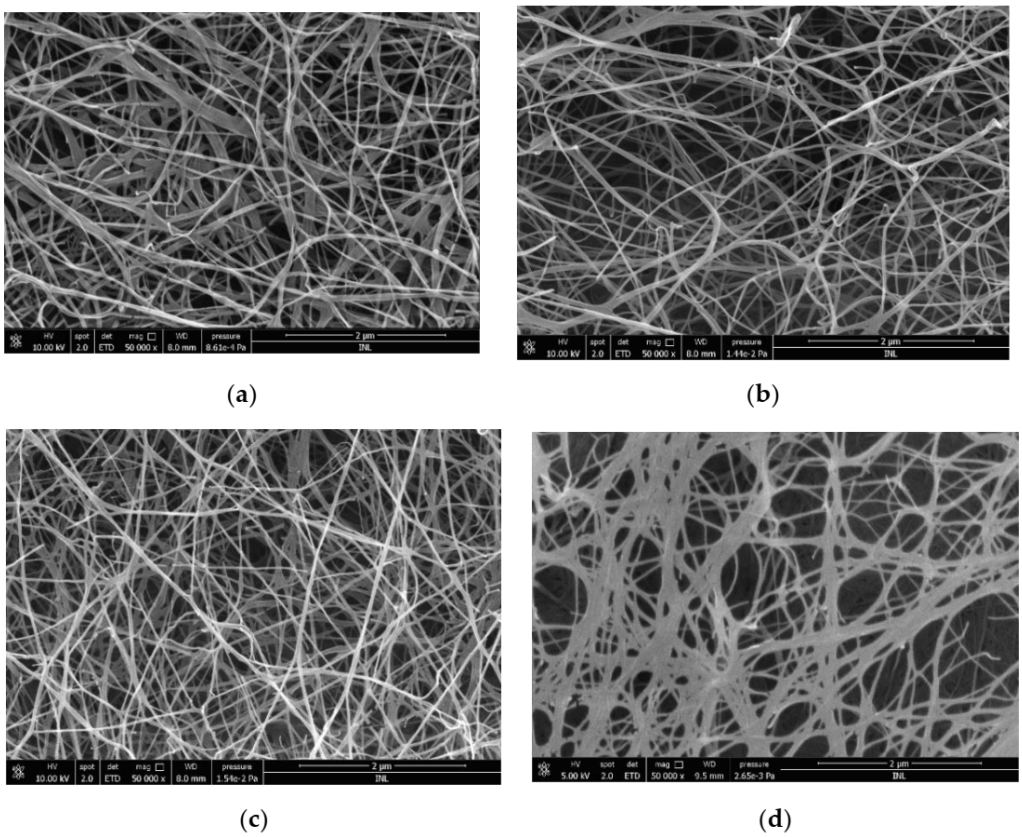

Figure 4. SEM images of (**a**) non-oxidized and (**b**) 400C, (**c**) 700C and (**d**) 1200C BNC membranes (magnification: 50,000×).

Table 2. Width of the oxidized and non-oxidized BNC fibers.

Sample	Width of the Fibers (nm)
Non-oxidized BNC	44.3 ± 2.14
BNC 400C	39.13 ± 2.04
BNC 700C	38.75 ± 1.15
BNC 1200C	29.56 ± 1.83

The SEM images revealed that oxidation did not affect the morphology of the fibers. The BNC exhibited the usual compact 3D-network structure of the nanofibrils, which remained almost similar after oxidation, showing that the electrochemical oxidation did not considerably affect their structure [48]. According to Table 2, the average width of the fibers was approximately 44 nm for pristine BNC, while for oxidized samples, the values varied between 29 nm and 39 nm, depending on the oxidation degree. Thus, the obtained values for both oxidized and non-oxidized samples were in accordance with the literature [49–51]. On the other hand, it was possible to observe that oxidation induced a slight decrease in the width of the fibers, although not so effective when compared to the work developed by Jun et al. [52], in which the average width of the fibers decreased from 100 nm to 30–50 nm after oxidation. Taking these results in account, we would expect a more expressive decrease in the width of the fibers, which was not observed.

3.7. XRD

Crystalline native cellulose exhibits high crystallinity, being a combination of two crystalline structures: triclinic (I_α) and monoclinic (I_β), which are present in distinct proportions, depending on the source. The first one is the major polymorph for most algae and bacteria, while the second one is dominant for higher-plant cell-wall cellulose, and

in tunicates [53]. XRD analyses were performed to understand the effect of oxidation on material crystallinity. Figure 5 shows the obtained diffractograms for the pristine and oxidized BNC samples with different oxidation degrees.

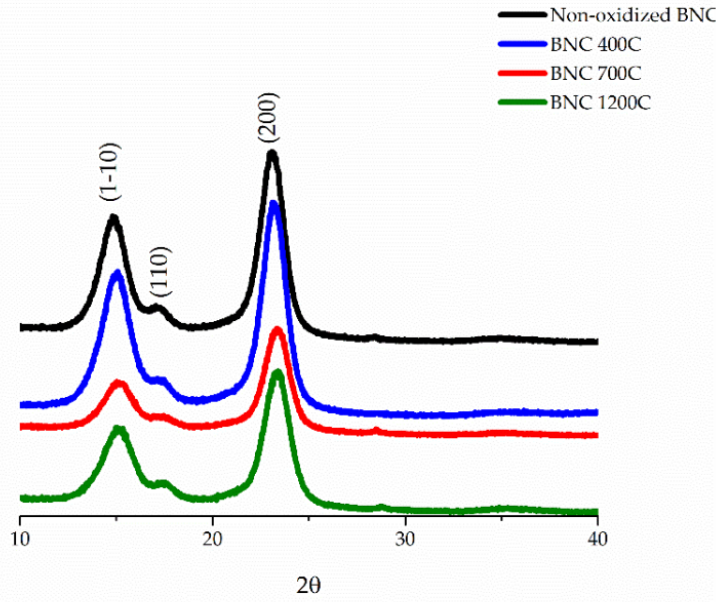

Figure 5. XRD patterns of oxidized and non-oxidized BNC membranes.

Pristine BNC exhibited diffraction peaks at 14.5°, 16.5° and 22.5°, corresponding to the primary diffraction of the crystal planes (1–10), (110) and (200), respectively, which is ascribed to cellulose I [54,55]. On the other hand, the obtained crystallinity indexes were very high for all samples (Table 3) and similar to those obtained by other authors [56,57].

Table 3. Crystallite size and crystallinity index of pristine and oxidized BNC.

Sample	Crystallite Size (nm)	Crystallinity Index (%)
Non-oxidized BNC	7.2	91.6
BNC 400C	6.9	89.4
BNC 700C	6.8	89.8
BNC 1200C	6.5	87.8

Table 3 also shows a slight decrease in the crystallinity index and in the crystallite size, related to an increase in oxidation degree [58,59], which may be explained by a destructuring effect of the cellulose intermolecular hydrogen bonds at the nanocrystallite surface [21]. Nevertheless, the diffraction peaks obtained for all the oxidized samples were very similar to pristine BNC membranes, suggesting that the oxidation process had a small effect on the crystal structure of the cellulose microfibrils [60].

3.8. In Vitro Degradation of Oxidized BNC Membranes

The degradation of BNC was assessed by gravimetry, after incubation of the samples in ultra-pure water for 3, 7, 14 and 63 days. The obtained results are presented in Figure 6.

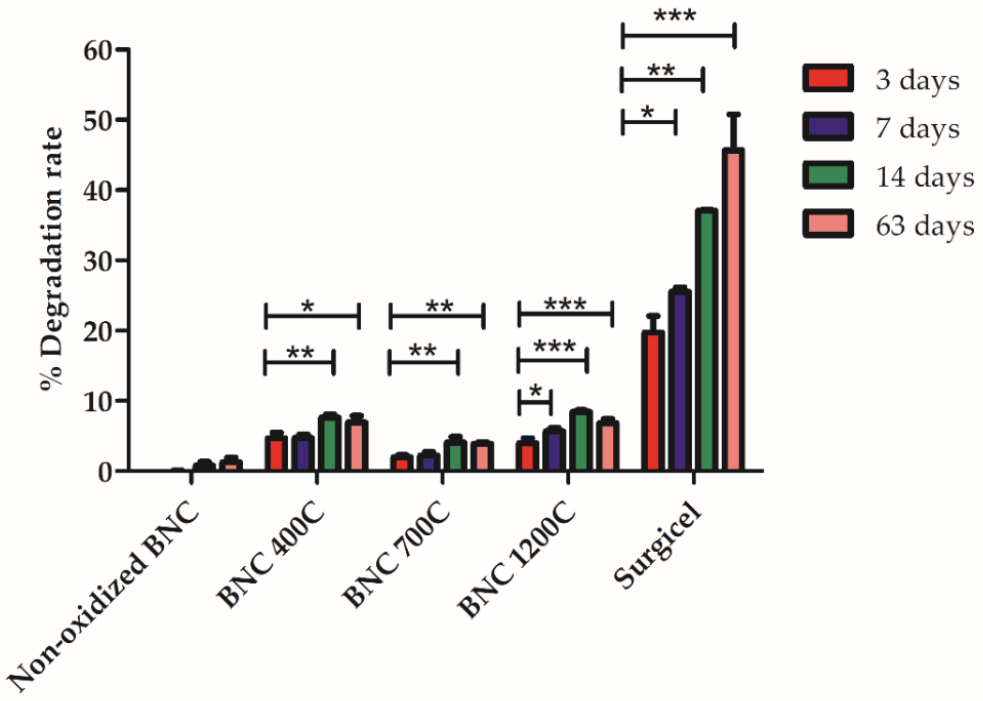

Figure 6. In vitro degradation of oxidized and non-oxidized BNC membranes. Significant differences are indicated as follows: * $p < 0.05$, ** $p < 0.01$ and *** $p < 0.001$.

As expected, the non-oxidized BNC did not degrade even after 63 days of incubation (the variation of the dry weight observed was not statistically significant). For all the oxidized samples and the Surgicel®, the degradation rate increased over time, revealing statistically significant differences ($p < 0.05$) from three days to the remaining time-points. However, unexpectedly, the BNC 700C degraded to a slightly lower extent compared to the BNC 400C, which in turn degraded to a similar extent as the BNC 1200C membranes, approximately 5% to 9%. In spite of these small differences, the degradation of the three membranes can be considered similar, with the comparison of the data corresponding to days 14 and 63 suggesting that the fraction of degradable oxidized cellulose was lower than 10%. On the other hand, Surgicel® degradation increased over time, but complete degradation did not occur even after 63 days of incubation. In the human body, Surgicel® is expected to fully degrade in a period of between 7 and 14 days [61]; however, in ultra-pure water, in vitro degradation achieved was only 46% after 63 days. The use of simulated body fluid (SBF) could provide a more realistic degradation rate [62,63], but we chose using ultra-pure water in the in vitro assays (degradation also was qualitatively monitored in vivo, as described below), since the degradation was monitored by gravimetry, and the residues from SBF could interfere in the results. The obtained results thus confirmed that oxidation improved the degradability of the BNC membranes. Since the BNC 1200C membrane was already quite fragile for the envisaged applications, we did not try to further increase the oxidation. We attributed the difficulty in achieving more extensive oxidation and biodegradability to the fact that the reaction occurred mainly on the surface of the fibers. This surface layer, oxidized to some extent, became degradable, but the inner layers were still non-biodegradable.

3.9. Biological Assays and Hemostatic Behavior of BNC Membranes

The whole-blood-clotting assay was applied to assess the pro-coagulative properties of the oxidized BNC. In this technique, fresh blood is placed in direct contact with BNC samples and, at different time-points, deionized water is added in order to promote the release of hemoglobin from those erythrocytes that are not immobilized in the forming

blood clot. This way, lower absorbance values are directly related with higher blood-clotting ability. The kinetics of the whole-blood clotting are presented in Figure 7.

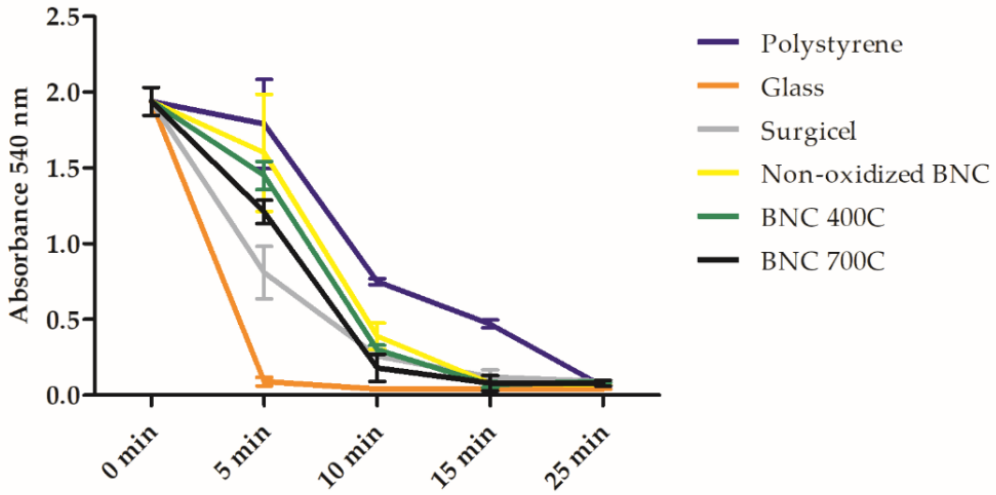

Figure 7. Whole-blood-clotting time using oxidized and non-oxidized BNC membranes.

Figure 7 displays the decrease of the absorbance values over time, showing that in every case, blood coagulation occurred within 25 min. The following relative behavior of the samples, from the highest to the lowest coagulation power, could be observed: glass microspheres > Surgicel® > oxidized BNC 700C > oxidized BNC 400C > non oxidized BNC > polystyrene. In accordance with Andrade et al. [64], the obtained results revealed that the BNC was slightly hemostatic, as compared to polystyrene. After oxidation, the BNC acquired improved hemostatic features, with the results obtained for BNC 700C being closer to those for the Surgicel®.

The hemostatic action of the oxidized BNC can be assigned to the negative charge provided by the carboxyl groups, which is known to start the blood-coagulation cascade by changing the conformation of the coagulation factor FXII upon adsorption. Indeed, the contact pathway can be started by negatively charged surfaces through the activation of the coagulation factors FXII, FXI, high-molecular-weight-kininogen (HMWK) and pre-kallikrein. It has been demonstrated that the adsorption of coagulation factor FXII might be more intense on negatively charged surfaces, governing its activation via positively charged amino acids on its heavy chain [65–68].

3.10. In Vivo Biocompatibility of BNC Membranes

The biocompatibility of the BNC membranes was assessed through their ability to induce irritation, inflammation or necrosis of the surrounding tissues in vivo. The samples were subcutaneously implanted in the rat, and the tissue response was evaluated.

In general, the implants preserved their location, size and shape until explantation (Figure 8). They could be easily identified and removed, since full degradation in vivo was not observed in any of the cases. After 3, 14 and 56 days of implantation, there were no macroscopic evidences of inflammation, such as redness, edema or exudates around the implanted BNC samples [17,18,35,69]. All the animals survived during the study period, and no infection or surgery-related complications occurred in either group.

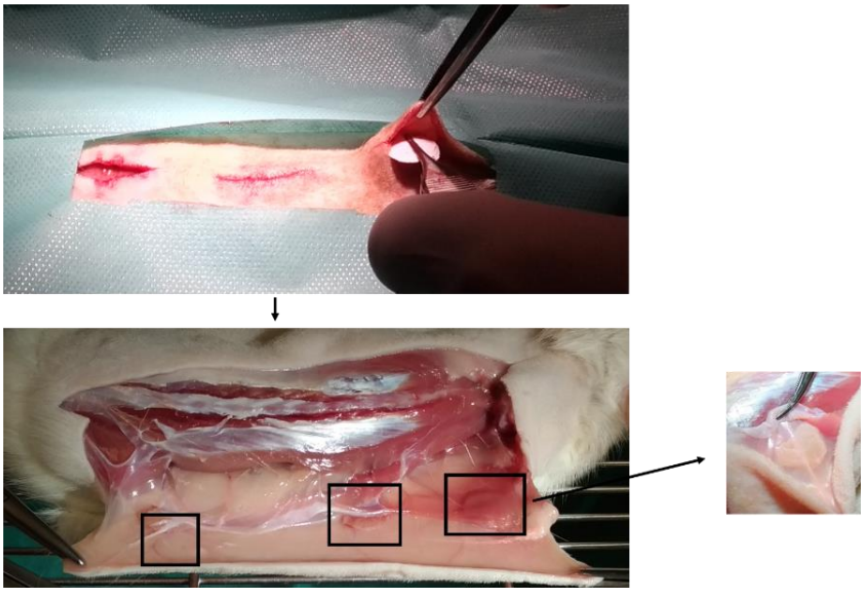

Figure 8. Photographs of the implantation and explantation process.

Histological assessment of the membranes was performed on days 3, 14 and 56 post-surgery. Histological images of the BNC membranes and surrounding tissues are presented in Figure 9, and the histological inflammation scores in Table 4.

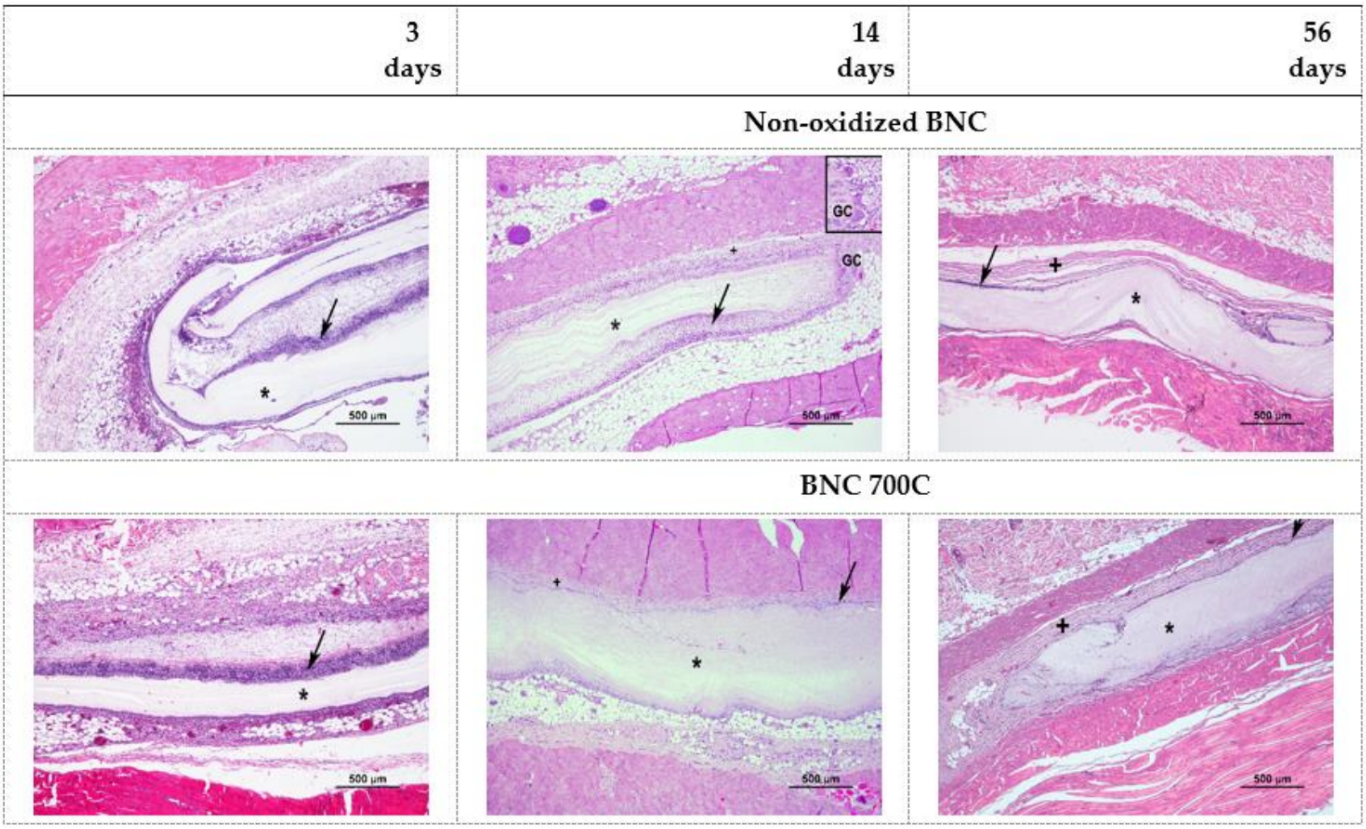

Figure 9. Histomorphology of oxidized and non-oxidized BNC membranes implanted subcutaneously in rat model (+ = fibrosis; black arrow = PMN; * = BNC; GC = giant cells).

Table 4. Histological assessment scores of oxidized and non-oxidized BNC membranes according to ISO standard 10993-6 (annex E).

	3 days		14 days		56 days	
	NO BNC	BNC 700C	NO BNC	BNC 700C	NO BNC	BNC 700C
Polymorphonuclear cells	4	2	3	2	1	1
Lymphocytes	2	2	2	2	2	2
Plasma cells	1	0	1	0	0	0
Macrophages	2	1	2	2	2	2
Giant cells	0	0	1	1	1	0
Necrosis	2	0	0	0	0	0
Neo vascularization	2	0	1	0	0	0
Fibrosis	0	0	1	3	3	4
Fatty infiltration	0	0	0	0	0	0

NO-BNC means non-oxidized BNC; 0 = Same as when implanted; 1 = Minimal; 2 = Mild; 3 = Moderate; 4 = Severe.

According to Figure 9 and Table 4, three days post-implantation, there was a predominance of neutrophils, lymphocytes, polymorphonuclear cells (PMN) and macrophages infiltrated at the implant–tissue interface in both experimental groups. However, the tissue reaction was more evident in non-oxidized samples comparing to oxidized ones, revealing that the acute response was more expressive in the former case. This was also confirmed by the presence of necrosis only in this experimental group. At days 14 and 56, the inflammatory reaction was still more expressive in the non-oxidized samples, with mononuclear cells being the predominant ones. As expected, fibrosis only occurred after 14 days of implantation, being more expressive after 56 days around the oxidized BNC membranes, which induced a higher fibroplasia. For all the time-points, the presence of giant cells was minimal, suggesting that the possible foreign-body reaction (FBR) would also be minimal. This was confirmed macroscopically, since the BNC membranes were well integrated with the rat connective tissue [35]. Even after 56 days of implantation, the oxidized membranes were still in place. Although the in vitro results showed that these samples degraded to a limited extent in 63 days, more extensive degradation was expected to occur in vivo. This cannot be quantified, but a significant fraction of material remained at the end of the trials.

Although the in vivo biocompatibility of BNC has been characterized by several authors [17,18,35,69–73], no studies have been performed to assess the behavior of oxidized BNC in vivo. Interestingly, the oxidized BNC seemed to attract fewer inflammatory cells than the pristine material, which is generally considered highly biocompatible, although it gives rise to a thicker fibrosis compared to non-oxidized samples.

4. Conclusions

Bacterial cellulose membranes were oxidized using electrochemical methods, and acquired hemostatic features and became partially degradable. The obtained results using FTIR and NMR techniques allowed us to conclude that the oxidation reaction occurred mainly at the surface layer of the cellulose fibers. Furthermore, both morphology and crystallinity of the oxidized membranes were preserved, although a slight reduction in crystallinity occurred after oxidation. This decrease in crystallinity was only around 4%, even for the samples with a higher oxidation degree, e.g., the pristine BNC had approximately 92%, while the oxidized sample had around 88%. The in vitro degradability of the oxidized membranes and their hemostatic potential were evaluated using Surgicel® as a control. The obtained results demonstrated that the oxidized BNC exhibited higher hemostatic activity than the pristine material, although not as effective as that of Surgicel®. The in vivo biodegradability and biocompatibility of oxidized membranes were assessed through subcutaneous implantation of the membranes in the rat, and showed a highly biocompatible behavior, triggering only a mild inflammation process. We hypothesize that a pre-treatment able to reduce BNC crystallinity followed by oxidation may yield a more oxidized, more biodegradable material that exhibits improved hemostatic features. This

will be the goal of further work aimed at developing BNC oxidized membrane dressings to prevent hemorrhagic episodes.

Author Contributions: Conceptualization, E.C.Q., P.P. and M.G.; methodology, E.C.Q.; validation, E.C.Q. and S.P.P.; formal analysis, E.C.Q. and S.P.P.; investigation, E.C.Q. and S.P.P.; resources, M.G., P.P., J.E.P., J.P., I.P. and F.D.; data curation, E.C.Q. and S.P.P.; writing—original draft preparation, E.C.Q.; writing—review and editing, E.C.Q., M.G., P.P. and F.D.; visualization, E.C.Q.; supervision, M.G and P.P.; project administration, M.G. and P.P.; funding acquisition, M.G. All authors have read and agreed to the published version of the manuscript.

Funding: This work was supported by the Fundação para a Ciência e Tecnologia (FCT), under the project BioTecNorte operation (NORTE01-0145-FEDER-000004), with funding by the European Regional Development Fund under the scope of Norte2020-Programa Operacional Regional do Norte.

Institutional Review Board Statement: The study was conducted according to the guidelines of the Declaration of Helsinki, and approved by Ethics Committee of Direcção Geral de Alimentação e Veterinária (DGAV, Lisboa, Portugal) (protocol code 0421/000/000/2017 and 2017/06/30).

Informed Consent Statement: Not applicable.

Data Availability Statement: Not applicable.

Acknowledgments: The authors gratefully give thanks to the project NORTE-08-5369-FSE-000012, with financial support of ESF—European Social Fund, under the scope of Norte2020—Programa Operacional Regional do Norte; and to UME-UTAD for the XRD analysis.

Conflicts of Interest: The authors declare no conflict of interest. The funders had no role in the design of the study; in the collection, analyses, or interpretation of data; in the writing of the manuscript; or in the decision to publish the results.

References

1. Bu, Y.; Zhang, L.; Sun, G.; Sun, F.; Liu, J.; Yang, F.; Tang, P.; Wu, D. Tetra-PEG Based Hydrogel Sealants for In Vivo Visceral Hemostasis. *Adv. Mater.* **2019**, *31*, 1901580. [CrossRef] [PubMed]
2. Yang, X.; Liu, W.; Shi, Y.; Xi, G.; Wang, M.; Liang, B.; Feng, Y.; Ren, X.; Shi, C. Peptide-Immobilized Starch/PEG Sponge with Rapid Shape Recovery and Dual-Function for Both Uncontrolled and Noncompressible Hemorrhage. *Acta Biomater.* **2019**, *99*, 220–235. [CrossRef] [PubMed]
3. Sirlak, M.; Eryilmaz, S.; Yazicioglu, L.; Kiziltepe, U.; Eyileten, Z.; Durdu, M.S.; Tasoz, R.; Eren, N.T.; Aral, A.; Kaya, B.; et al. Comparative Study of Microfibrillar Collagen Hemostat (Colgel) and Oxidized Cellulose (Surgicel) in High Transfusion-Risk Cardiac Surgery. *J. Thorac. Cardiovasc. Surg.* **2003**, *126*, 666–670. [CrossRef]
4. Gabay, M.; Boucher, B.A. An Essential Primer for Understanding the Role of Topical Hemostats, Surgical Sealants, and Adhesives for Maintaining Hemostasis. *Pharmacotherapy* **2013**, *33*, 935–955. [CrossRef] [PubMed]
5. Agarwal, M.M.; Mandal, A.K.; Agarwal, S.; Lal, A.; Prakash, M.; Mavuduru, R.; Singh, S.K. Surgicel Granuloma: Unusual Cause of "Recurrent" Mass Lesion after Laparoscopic Nephron-Sparing Surgery for Renal Cell Carcinoma. *Urology* **2010**, *76*, 334–335. [CrossRef] [PubMed]
6. Alpaslan, C.; Alpaslan, G.H.; Oygur, T. Tissue Reaction to Three Subcutaneously Implanted Local Hemostatic Agents. *Br. J. Oral Maxillofac. Surg.* **1997**, *35*, 129–132. [CrossRef]
7. Wang, H.; Chen, P. Surgicel® (Oxidized Regenerated Cellulose) Granuloma Mimicking Local Recurrent Gastrointestinal Stromal Tumor: A Case Report. *Oncol. Lett.* **2013**, *5*, 1497–1500. [CrossRef] [PubMed]
8. Ibrahim, M.F.; Aps, C.; Young, C.P. A Foreign Body Reaction to Surgicel Mimicking an Abscess Following Cardiac Surgery. *Eur. J. Cardiothorac. Surg.* **2002**, *22*, 489–490. [CrossRef]
9. Lin, B.; Yang, H.; Cui, M.; Li, Y.; Yu, J. Surgicel™ Application in Intracranial Hemorrhage Surgery Contributed to Giant-Cell Granuloma in a Patient with Hypertension: Case Report and Review of the Literature. *World J. Surg. Oncol.* **2014**, *12*, 101. [CrossRef] [PubMed]
10. Portela, R.; Leal, C.R.; Almeida, P.L.; Sobral, R.G. Bacterial Cellulose: A Versatile Biopolymer for Wound Dressing Applications. *Microb. Biotechnol.* **2019**, *12*, 586–610. [CrossRef] [PubMed]
11. Pang, M.; Huang, Y.; Meng, F.; Zhuang, Y.; Liu, H.; Du, M.; Ma, Q.; Wang, Q.; Chen, Z.; Chen, L.; et al. Application of Bacterial Cellulose in Skin and Bone Tissue Engineering. *Eur. Polym. J.* **2020**, *122*, 109365. [CrossRef]
12. Gorgieva, S.; Trček, J. Bacterial Cellulose: Production, Modification and Perspectives in Biomedical Applications. *Nanomaterials* **2019**, *9*, 1352. [CrossRef]
13. Eslahi, N.; Mahmoodi, A.; Mahmoudi, N.; Zandi, N.; Simchi, A. Processing and Properties of Nanofibrous Bacterial Cellulose-Containing Polymer Composites: A Review of Recent Advances for Biomedical Applications. *Polym. Rev.* **2020**, *60*, 144–170. [CrossRef]

14. Volova, T.G.; Prudnikova, S.V.; Sukovatyi, A.G.; Shishatskaya, E.I. Production and Properties of Bacterial Cellulose by the Strain Komagataeibacter Xylinus B-12068. *Appl. Microbiol. Biotechnol.* **2018**, *102*, 7417–7428. [CrossRef]
15. Uzyol, H.K.; Saçan, M.T. Bacterial Cellulose Production by Komagataeibacter Hansenii Using Algae-Based Glucose. *Environ. Sci. Pollut. Res.* **2017**, *24*, 11154–11162. [CrossRef] [PubMed]
16. Klemm, D.; Heublein, B.; Fink, H.P.; Bohn, A. Cellulose: Fascinating Biopolymer and Sustainable Raw Material. *Angew. Chemie Int. Ed.* **2005**, *44*, 3358–3393. [CrossRef] [PubMed]
17. Helenius, G.; Bäckdahl, H.; Bodin, A.; Nannmark, U.; Gatenholm, P.; Risberg, B. In Vivo Biocompatibility of Bacterial Cellulose. *J. Biomed. Mater. Res. Part A* **2006**, *76*, 431–438. [CrossRef]
18. Pértile, R.A.N.; Moreira, S.; Gil Da Costa, R.M.; Correia, A.; Guardão, L.; Gartner, F.; Vilanova, M.; Gama, M. Bacterial Cellulose: Long-Term Biocompatibility Studies. *J. Biomater. Sci. Polym. Ed.* **2012**, *23*, 1339–1354. [CrossRef]
19. Zhang, C.; Cao, J.; Zhao, S.; Luo, H.; Yang, Z.; Gama, M.; Zhang, Q.; Su, D.; Wan, Y. Biocompatibility Evaluation of Bacterial Cellulose as a Scaffold Material for Tissue-Engineered Corneal Stroma. *Cellulose* **2020**, *27*, 2775–2784. [CrossRef]
20. Camy, S.; Montanari, S.; Rattaz, A.; Vignon, M.; Condoret, J.S. Oxidation of Cellulose in Pressurized Carbon Dioxide. *J. Supercrit. Fluids* **2009**, *51*, 188–196. [CrossRef]
21. Liao, S.B.; Xi, T.F.; Lai, C.; Liao, S.Y.; Huang, T.; Wang, S.Y. TEMPO-Mediated Oxidation of Bacterial Cellulose in a Bromide-Free System. *Colloid Polym. Sci.* **2013**, *32*, 699–707. [CrossRef]
22. Davis, N.J.; Flitsch, S.L. Selective Oxidation of Monosaccharide Derivatives to Uronic Acids. *Tetrahedron Lett.* **1993**, *34*, 1181–1184. [CrossRef]
23. Pahlevan, M.; Toivakka, M.; Alam, P. Mechanical Properties of TEMPO-Oxidised Bacterial Cellulose-Amino Acid Biomaterials. *Eur. Polym. J.* **2018**, *101*, 29–36. [CrossRef]
24. Lai, C.; Sheng, L.; Liao, S.; Xi, T.; Zhang, Z. Surface Characterization of TEMPO-Oxidized Bacterial Cellulose. *Surf. Interface Anal.* **2013**, *45*, 1673–1679. [CrossRef]
25. Isogai, A.; Kato, Y. Preparation of Polyuronic Acid from Cellulose by TEMPO-Mediated Oxidation. *Cellulose* **1998**, *5*, 153–164. [CrossRef]
26. Bragd, P.L.; van Bekkum, H.; Besemer, A.C. TEMPO-Mediated Oxidation of Polysaccharides: Survey of Methods and Applications. *Top. Catal.* **2004**, *27*, 49–66. [CrossRef]
27. Carlsson, D.O.; Lindh, J.; Nyholm, L.; Stromme, M.; Mihranyan, A.; Strømme, M.; Mihranyan, A. Cooxidant-Free TEMPO-Mediated Oxidation of Highly Crystalline Nanocellulose in Water. *RSC Adv.* **2014**, *4*, 52289–52298. [CrossRef]
28. Parpot, P.; Servat, K.; Bettencourt, A.P.; Huser, H.; Kokoh, K.B. TEMPO Mediated Oxidation of Carbohydrates Using Electrochemical Methods. *Cellulose* **2010**, *17*, 815–824. [CrossRef]
29. Cui, Q.; Zheng, Y.; Lin, Q.; Song, W.; Qiao, K.; Liu, S. Selective Oxidation of Bacterial Cellulose by NO_2-HNO_3. *RSC Adv.* **2014**, *4*, 1630–1639. [CrossRef]
30. Evans, R.; Wallis, A.F.A. Cellulose Molecular Weights Determined by Viscometry. *J. Appl. Polym. Sci.* **1989**, *37*, 2331–2340. [CrossRef]
31. Tsouko, E.; Kourmentza, C.; Ladakis, D.; Kopsahelis, N.; Mandala, I.; Papanikolaou, S.; Paloukis, F.; Alves, V.; Koutinas, A. Bacterial Cellulose Production from Industrial Waste and By-Product Streams. *Int. J. Mol. Sci.* **2015**, *16*, 14832–14849. [CrossRef]
32. Ryu, D.D.Y.; Lee, S.B.; Tassinari, T.; Macy, C. Effect of Compression Milling on Cellulose Structure and on Enzymatic Hydrolysis Kinetics. *Biotechnol. Bioeng.* **1982**, *24*, 1047–1067. [CrossRef]
33. Segal, L.; Creely, J.J.; Martin, A.E.; Conrad, C.M. An Empirical Method for Estimating the Degree of Crystallinity of Native Cellulose Using the X-Ray Diffractometer. *Text. Res. J.* **1959**, *29*, 786–794. [CrossRef]
34. Leitão, A.F.; Silva, J.P.; Dourado, F.; Gama, M. Hemocompatibility Study of a Bacterial Cellulose/Poly(Vinyl Alcohol) Nanocomposite. *Colloids Surf. B Biointerfaces* **2013**, *6*, 493–502. [CrossRef] [PubMed]
35. Andrade, F.K.; Alexandre, N.; Amorim, I.; Gartner, F.; Maurício, A.C.; Luís, A.L.; Gama, M. Studies on the Biocompatibility of Bacterial Cellulose. *J. Bioact. Compat. Polym.* **2013**, *28*, 97–112. [CrossRef]
36. Zhang, Y.; Zhou, Z.; Wen, F.; Yuan, K.; Tan, J.; Zhang, Z.; Wang, H. Tubular Structured Bacterial Cellulose-Based Nitrite Sensor: Preparation and Environmental Application. *J. Solid State Electrochem.* **2017**, *21*, 3649–3657. [CrossRef]
37. Zaid, M.H.M.; Abdullah, J.; Yusof, N.A.; Wasoh, H.; Sulaiman, Y.; Noh, M.F.M.; Issa, R. Reduced Graphene Oxide/TEMPO-Nanocellulose Nanohybrid-Based Electrochemical Biosensor for the Determination of Mycobacterium Tuberculosis. *J. Sens.* **2020**, *2020*, 1–11. [CrossRef]
38. Gomes, N.O.; Carrilho, E.; Machado, S.A.S.; Sgobbi, L.F. Bacterial Cellulose-Based Electrochemical Sensing Platform: A Smart Material for Miniaturized Biosensors. *Electrochim. Acta* **2020**, *349*, 136341. [CrossRef]
39. Sezer, U.A.; Sahin, İ.; Aru, B.; Olmez, H.; Demirel, G.Y.; Sezer, S. Cytotoxicity, Bactericidal and Hemostatic Evaluation of Oxidized Cellulose Microparticles: Structure and Oxidation Degree Approach. *Carbohydr. Polym.* **2019**, *219*, 87–94. [CrossRef]
40. Saito, T.; Isogai, A. TEMPO-Mediated Oxidation of Native Cellulose. The Effect of Oxidation Conditions on Chemical and Crystal Structures of the Water-Insoluble Fractions. *Biomacromolecules* **2004**, *5*, 1983–1989. [CrossRef]
41. Hiraoki, R.; Ono, Y.; Saito, T.; Isogai, A. Molecular Mass and Molecular-Mass Distribution of TEMPO-Oxidized Celluloses and TEMPO-Oxidized Cellulose Nanofibrils. *Biomacromolecules* **2015**, *16*, 675–681. [CrossRef] [PubMed]
42. Fukuzumi, H.; Saito, T.; Isogai, A. Influence of TEMPO-Oxidized Cellulose Nanofibril Length on Film Properties. *Carbohydr. Polym.* **2013**, *93*, 172–177. [CrossRef] [PubMed]

43. Neves, R.M.; Lopes, K.S.; Zimmermann, M.G.V.; Poletto, M.; Zattera, A.J. Cellulose Nanowhiskers Extracted from Tempo-Oxidized Curaua Fibers. *J. Nat. Fibers* **2020**, *17*, 1355–1365. [CrossRef]
44. Sang, X.; Qin, C.; Tong, Z.; Kong, S.; Jia, Z.; Wan, G.; Liu, X. Mechanism and Kinetics Studies of Carboxyl Group Formation on the Surface of Cellulose Fiber in a TEMPO-Mediated System. *Cellulose* **2017**, *24*, 2415–2425. [CrossRef]
45. Tang, R.; Yu, Z.; Renneckar, S.; Zhang, Y. Coupling Chitosan and TEMPO-Oxidized Nanofibrilliated Cellulose by Electrostatic Attraction and Chemical Reaction. *Carbohydr. Polym.* **2018**, *202*, 84–90. [CrossRef]
46. Lai, C.; Zhang, S.; Chen, X.; Sheng, L. Nanocomposite Films Based on TEMPO-Mediated Oxidized Bacterial Cellulose and Chitosan. *Cellulose* **2014**, *21*, 2757–2772. [CrossRef]
47. do Nascimento, E.S.; Pereira, A.L.S.; De Oliveira Barros, M.; De Aaraújo Barroso, M.K.; Lima, H.L.S.; De Fátima Borges, M.; De Andrade Feitosa, J.P.; de Azeredo, H.M.C.; De Freitas Rosa, M. TEMPO Oxidation and High-Speed Blending as a Combined Approach to Disassemble Bacterial Cellulose. *Cellulose* **2019**, *26*, 2291–2302. [CrossRef]
48. Luo, H.; Xiong, G.; Hu, D.; Ren, K.; Yao, F.; Zhu, Y.; Gao, C.; Wan, Y. Characterization of TEMPO-Oxidized Bacterial Cellulose Scaffolds for Tissue Engineering Applications. *Mater. Chem. Phys.* **2013**, *143*, 373–379. [CrossRef]
49. Klemm, D.; Kramer, F.; Moritz, S.; Lindström, T.; Ankerfors, M.; Gray, D.; Dorris, A. Nanocelluloses: A New Family of Nature-Based Materials. *Angew. Chem. Int. Ed.* **2011**, *50*, 5438–5466. [CrossRef]
50. Wang, J.; Tavakoli, J.; Tang, Y. Bacterial Cellulose Production, Properties and Applications with Different Culture Methods—A Review. *Carbohydr. Polym.* **2019**, *219*, 63–76. [CrossRef]
51. Numata, Y.; Kono, H.; Mori, A.; Kishimoto, R.; Tajima, K. Structural and Rheological Characterization of Bacterial Cellulose Gels Obtained from Gluconacetobacter Genus. *Food Hydrocoll.* **2019**, *92*, 233–239. [CrossRef]
52. Jun, S.H.; Park, S.G.; Kang, N.G. One-Pot Method of Synthesizing TEMPO-Oxidized Bacterial Cellulose Nanofibers Using Immobilized TEMPO for Skincare Applications. *Polymers* **2019**, *11*, 1044. [CrossRef] [PubMed]
53. Horii, F.; Hirai, A.; Yamamoto, H. Microstructural Analysis of Microfibrils of Bacterial Cellulose. *Macromol. Symp.* **1997**, *120*, 197–205. [CrossRef]
54. Vasconcelos, N.F.; Feitosa, J.P.A.; da Gama, F.M.P.; Morais, J.P.S.; Andrade, F.K.; de Souza Filho, M.d.S.M.; De Freitas Rosa, M. Bacterial Cellulose Nanocrystals Produced under Different Hydrolysis Conditions: Properties and Morphological Features. *Carbohydr. Polym.* **2017**, *155*, 425–431. [CrossRef] [PubMed]
55. Vasconcelos, N.F.; Andrade, F.K.; De Araújo Pinto Vieira, L.; Vieira, R.S.; Vaz, J.M.; Chevallier, P.; Mantovani, D.; De Fátima Borges, M.; De Freitas Rosa, M. Oxidized Bacterial Cellulose Membrane as Support for Enzyme Immobilization: Properties and Morphological Features. *Cellulose* **2020**, *27*, 3055–3083. [CrossRef]
56. Kashcheyeva, E.I.; Gladysheva, E.K.; Skiba, E.A.; Budaeva, V.V. A Study of Properties and Enzymatic Hydrolysis of Bacterial Cellulose. *Cellulose* **2019**, *26*, 2255–2265. [CrossRef]
57. Cheng, K.C.; Catchmark, J.M.; Demirci, A. Effect of Different Additives on Bacterial Cellulose Production by Acetobacter Xylinum and Analysis of Material Property. *Cellulose* **2009**, *16*, 1033–1045. [CrossRef]
58. Li, J.; Wan, Y.; Li, L.; Liang, H.; Wang, J. Preparation and Characterization of 2,3-Dialdehyde Bacterial Cellulose for Potential Biodegradable Tissue Engineering Scaffolds. *Mater. Sci. Eng. C* **2009**, *29*, 1635–1642. [CrossRef]
59. Li, H.; Wu, B.; Mu, C.; Lin, W. Concomitant Degradation in Periodate Oxidation of Carboxymethyl Cellulose. *Carbohydr. Polym.* **2011**, *84*, 881–886. [CrossRef]
60. Peng, S.; Zheng, Y.; Wu, J.; Wu, Y.; Ma, Y.; Song, W.; Xi, T. Preparation and Characterization of Degradable Oxidized Bacterial Cellulose Reacted with Nitrogen Dioxide. *Polym. Bull.* **2012**, *68*, 415–423. [CrossRef]
61. Dan Dimitrijevich, S.; Tatarko, M.; Gracy, R.W.; Linsky, C.B.; Olsen, C. Biodegradation of Oxidized Regenerated Cellulose. *Carbohydr. Res.* **1990**, *195*, 247–256. [CrossRef]
62. Wan, Y.; Chen, Y.; Xi, T.; Zheng, Y.; Zhou, L. In Vitro Structural Changes of Nano-Bacterial Cellulose Immersed in Phosphate Buffer Solution In Vitro Structural Changes of Nano-Bacterial Cellulose Immersed in Phosphate Buffer Solution. *Artic. J. Biomim. Biomater. Tissue Eng.* **2011**, *10*, 55–66. [CrossRef]
63. Shi, X.; Cui, Q.; Zheng, Y.; Peng, S.; Wang, G.; Xie, Y. Effect of Selective Oxidation of Bacterial Cellulose on Degradability in Phosphate Buffer Solution and Their Affinity for Epidermal Cell Attachment. *RSC Adv.* **2014**, *4*, 60749–60756. [CrossRef]
64. Andrade, F.K.; Moreira, S.M.G.; Domingues, L.; Gama, F.M.P. Improving the Affinity of Fibroblasts for Bacterial Cellulose Using Carbohydrate-Binding Modules Fused to RGD. *J. Biomed. Mater. Res. Part A* **2010**, *92*, 9–17. [CrossRef] [PubMed]
65. Sperling, C.; Fischer, M.; Maitz, M.F.; Werner, C. Blood Coagulation on Biomaterials Requires the Combination of Distinct Activation Processes. *Biomaterials* **2009**, *30*, 4447–4456. [CrossRef] [PubMed]
66. Palta, S.; Saroa, R.; Palta, A. Overview of the Coagulation System. *Indian J. Anaesth.* **2014**, *58*, 515–523. [CrossRef] [PubMed]
67. Zhang, S.; Li, J.; Chen, S.; Zhang, X.; Ma, J.; He, J. Oxidized Cellulose-Based Hemostatic Materials. *Carbohydr. Polym.* **2020**, *230*, 115585. [CrossRef] [PubMed]
68. Yuan, H.; Chen, L.; Hong, F.F. A Biodegradable Antibacterial Nanocomposite Based on Oxidized Bacterial Nanocellulose for Rapid Hemostasis and Wound Healing. *ACS Appl. Mater. Interfaces* **2020**, *12*, 3382–3392. [CrossRef]
69. De, L.; Holgado, A.; Leao, A.; Rodrigues, M.; Chaves, M.; Kinoshita, A. Tissue Reaction after Subcutaneous Implantation of a Membrane Composed of Bacterial Cellulose Embedded with Hydroxyapatite. *Dent. Oral Craniofac. Res.* **2015**, *1*, 25–30. [CrossRef]

70. Huang, L.; Du, X.; Fan, S.; Yang, G.; Shao, H.; Li, D.; Cao, C.; Zhu, Y.; Zhu, M.; Zhang, Y. Bacterial Cellulose Nanofibers Promote Stress and Fidelity of 3D-Printed Silk Based Hydrogel Scaffold with Hierarchical Pores. *Carbohydr. Polym.* **2019**, *221*, 146–156. [CrossRef]
71. Kumbhar, J.V.; Jadhav, S.H.; Bodas, D.S.; Barhanpurkar-Naik, A.; Wani, M.R.; Paknikar, K.M.; Rrajwade, J.M. In Vitro and In Vivo Studies of a Novel Bacterial Cellulose-Based Acellular Bilayer Nanocomposite Scaffold for the Repair of Osteochondral Defects. *Int. J. Nanomed.* **2017**, *12*, 6437–6459. [CrossRef] [PubMed]
72. De Lima, F.M.T.; Pinto, F.C.M.; Andrade-da-Costa, B.L.d.S.; da Silva, J.G.M.; Júnior, O.C.; De Andrade Aguiar, J.L. Biocompatible Bacterial Cellulose Membrane in Dural Defect Repair of Rat. *J. Mater. Sci. Mater. Med.* **2017**, *28*, 37. [CrossRef] [PubMed]
73. Wang, B.; Lv, X.; Chen, S.; Li, Z.; Sun, X.; Feng, C.; Wang, H.; Xu, Y. In Vitro Biodegradability of Bacterial Cellulose by Cellulase in Simulated Body Fluid and Compatibility in Vivo. *Cellulose* **2016**, *23*, 3187–3198. [CrossRef]